

# Near-Real Time Thermospheric Density Retrieval from Precise Low Earth Orbit Spacecraft Ephemerides During Geomagnetic Storms

Charles Constant<sup>1</sup>, Santosh Bhattarai<sup>1</sup>, Indigo Brownhall<sup>1</sup>, Anasuya Aruliah<sup>2</sup>,  
Marek Ziebart<sup>1</sup>

<sup>1</sup>University College London, Space Geodesy and Navigation Laboratory

<sup>2</sup>University College London, Atmospheric Physics Laboratory

<sup>1</sup>Gower Street, WC1E 6BT, London

<sup>2</sup>Gower Street, WC1E 6BT, London

## Key Points:

- Current operational thermospheric models struggle to compute storm-time behavior, degrading orbit predictions during high solar activity.
- New data-assimilative and physics-based models offer better accuracy but face restricted access and operational limitations.
- High-resolution storm-time density estimates can be extracted in near-real time from freely available precise orbit data.

arXiv:2408.16805v1 [physics.space-ph] 29 Aug 2024

---

Corresponding author: Charles Constant, [zcesccc@ucl.ac.uk](mailto:zcesccc@ucl.ac.uk)

## Abstract

We present a methodology to generate low-latency, high spatio-temporal resolution thermospheric density estimates using publicly available Low Earth Orbit (LEO) spacecraft ephemerides. This provides a means of generating density estimates that can be used in a data-assimilative context by the satellite operations and thermosphere communities. It also contributes to the database of high-resolution density estimates during geomagnetic storms- which remains one of the major gaps for the development and benchmarking of density models.

Using accelerometer-derived densities from the Gravity Recovery And Climate Experiment Follow-On (GRACE-FO) spacecraft as truth, our method surpasses Energy Dissipation Rate-Type density retrieval techniques and three widely used operational density models in terms of mean absolute percentage error: EDR (103.37%), JB2008 (85.43%), DTM2000 (52.73%), and NRLMSISE-00 (12.31%).

We demonstrate the robustness of our methodology during a critical time for spacecraft operators- attempting to operate in the presence of geomagnetic storms, by reconstructing density profiles along the orbits of three LEO satellites during 80 geomagnetic storms over the last two decades (2001-2024). These profiles exhibit high spatial and temporal resolution compared to three operational thermospheric models, highlighting the operational applicability and potential for their use in model validation.

Our findings suggest that the increasing availability of precise orbit determination data offers a valuable, yet underutilized, resource that could provide a significant improvement to data assimilative thermospheric models, ultimately enhancing both spacecraft operations and thermospheric modeling efforts.

## 1 Introduction

The proliferation of satellites in Low Earth Orbit (LEO) coupled with the intensified solar activity characteristic of the current solar cycle (number 25) poses significant challenges for spacecraft operations (Berger et al., 2023). The inadequacy of existing atmospheric density models to accurately capture the thermosphere’s storm-time behavior exacerbates these challenges (Oliveira et al., 2017; He et al., 2023; Bussy-Virat et al., 2018). This inadequacy leads to the degradation of orbital products used in space traffic management, and even occasionally culminating in uncontrolled spacecraft re-entries (Fang et al., 2022).

Current non-proprietary operational thermospheric density models, such as Jacchia-Bowman 2008 (JB2008), Drag Temperature Model 2000 (DTM2000) and Naval Research Laboratory Mass Spectrometer and Incoherent Scatter Radar Exosphere 2000 (NRLMSISE-00), are empirical (Gondelach & Linares, 2020; Foster et al., 2016; Fang et al., 2022). These models employ mathematical parameterizations, including Fourier Series, constrained by physical laws to model averaged observational data. They are computationally efficient, and their performance is well-understood within the community. Although these empirical models capture the general features of thermospheric behavior (e.g. diurnal bulge), their spatio-temporal resolution of thermospheric features is limited (He et al., 2023; Oliveira et al., 2021). For instance, few empirical models capture the density enhancements associated with Joule heating and neutral winds (Brown & Elvidge, 2024). The necessity for higher spatio-temporal resolution within such models is becoming critical for satellite operators (Fang et al., 2022; Berger et al., 2023).

Data-assimilation methods have been developed to mitigate the limitations of current atmospheric density models (Sutton, 2018; Gondelach & Linares, 2020; Matsuo et al., 2012). These methods leverage near-real-time measurements to enhance model accuracy. A notable example is the High Accuracy Satellite Drag Model (HASDM) at the

Combined Space Operations Center (Storz, 2002; Picone et al., 2005). Widely regarded as state-of-the-art (Berger et al., 2023), HASDM’s solutions, however, degrade over time as they remain constrained by the limitations of the model they update: JB2008 (Licata et al., 2021). Continuous radar tracking of approximately 80 calibration objects is necessary, with updates to the model occurring only every three hours (S. Mutschler et al., 2023; Storz, 2002). While beneficial for the Combined Space Operations Center, this approach is impractical for individual spacecraft operators due to the extensive tracking requirements. Moreover, operational access to HASDM is predominantly restricted to the U.S. government (S. Mutschler et al., 2023).

Other data-assimilative models are currently under development within the community (Pilinski, McNally, et al., 2016; Sutton, 2018; Elvidge & Angling, 2019); however, none have reached the stage of being used as part of an operational pipeline or system (i.e. employed in orbit prediction or determination by satellite operators or Space Situational Awareness/Space Traffic Management (SSA/STM) organizations).

A different class of models, previously considered too computationally intensive for practical use in satellite operations, is becoming increasingly viable: physics-based models. These models, which solve the Navier-Stokes and diffusion equations for parameters such as density, velocity, and temperature of the thermosphere along the air column (Gondelach & Linares, 2020), offer higher resolution and greater flexibility compared to empirical models. The development of these models marks significant progress in accurately representing the complexities of the thermospheric environment, demonstrating how far physics-based modeling has come in recent years (Brown & Elvidge, 2024; Codrescu et al., 2012; Bruinsma et al., 2023). Substantial work remains to further refine these models. This includes optimizing the models to reduce computational costs while maintaining accuracy, and enhancing their adaptability for real-time data assimilation and forecasting (Sutton, 2018; S. Mutschler et al., 2023; Elvidge & Angling, 2019; Mehta & Linares, 2018).

A common limitation of all current models is the paucity of observational data for validation. In-situ mass spectrometer measurements of thermospheric density and composition are extremely limited (Siemes et al., 2022; Bruinsma et al., 2023). Consequently, most models are validated using spacecraft orbit data, making it challenging to distinguish between errors arising from orbit propagation and those related to model-resolved densities. Indirect measurements continue to provide the majority of thermospheric density observations. Historically, these methods have relied on monitoring satellite decay rates over multiple orbits (King-Hele & Walker, 1987; Saunders et al., 2011; B. R. Bowman et al., 2005; Picone et al., 2005), resulting in biased and low-resolution estimates (Mehta et al., 2017).

Over the past two decades, novel methods have been developed to overcome the limitations of traditional techniques. Two-Line Element (TLE)-centric methods have gained popularity due to the widespread availability of TLE data (Doornbos et al., 2008; Gondelach & Linares, 2020; Storz, 2002). However, these methods are constrained by the low accuracy and high latency characteristic of the TLE data publication process. Machine learning approaches have also been employed to enhance model accuracy (Briden et al., 2022; Mehta et al., 2017), but these improvements are limited by the quality and sparsity of the training data and do not address the issue of spatio-temporal resolution. Accelerometer-derived density retrieval is regarded as the gold standard for spatio-temporal resolution and accuracy (van den IJssel et al., 2020; Doornbos, 2011; Siemes et al., 2024), yet it is restricted to a few scientific missions equipped with the necessary accelerometers (e.g., CHAMP, GRACE, SWARM, GOCE).

More recently, precise orbit ephemerides have emerged as valuable sources of indirect density measurements (Kuang et al., 2014; Calabria & Jin, 2017; van den IJssel et al., 2020; Ray et al., 2023). The increasing adoption of open practices in scientific and even commercial missions, driven by the demand for transparency in the space traffic

management community (Larsen, 2008; Lal et al., 2018; Robinson, 2016), has significantly expanded the availability of precise ephemerides (Arnold et al., 2023; Foster et al., 2016; Schreiner et al., 2022).

The pool of precise spacecraft data is not only expanding, but the quality of available LEO ephemeris data has also improved significantly in recent years. Almost 90% of LEO Precise Orbit Determination (POD) studies over the past two decades report accuracies below the 10 cm level (Selvan et al., 2023). This decimeter-level accuracy meets the requirements for ephemeris-based density inversion in LEO (Ray et al., 2023), highlighting the increasing potential for the growing number of satellites in LEO to function as thermosphere sensors.

The latest International Space Weather Action Teams Working Meeting (Mehta et al., 2022) called for:

1. High-quality density data. It was identified as a limiting factor in the development of empirical atmospheric density models.
2. New ways of achieving “high-resolution monitoring of geomagnetic storms” as current databases “severely penalize both modeling and model assessment”.

The following work aims to enhance the accessibility and application of ephemeris-based density estimation, particularly during geomagnetic storms. Building on previous research (Calabia et al., 2015; Calabia & Jin, 2017, 2021; Ray et al., 2023), we have developed and applied a method using rapid science and near-real-time orbit data from GeoForschungsZentrum Potsdam (Schreiner et al., 2022). Our method computes density at a rate of more than once per second across three LEO spacecraft, assessed across 80 geomagnetic storms. Practically speaking, the additional delay incurred by the application of this method to the POD data streams ranges from a handful of seconds to tens of minutes depending on available compute and selected resolution.

Our findings demonstrate that this method can resolve storm-time density with spatio-temporal resolution approaching that of accelerometer derived densities, surpassing the accuracy of operational density models in many cases and approaching the resolution of accelerometer data, provided the Signal-to-Noise Ratio (SNR) in the drag signal is sufficiently strong. An in-depth analysis of the required SNR for different POD-based density retrieval methods is outlined in (Ray et al., 2023).

## 2 Methodology

### 2.1 Spacecraft and Orbit Source selection

A primary objective of the methodology developed in this study was to enhance the operational applicability of density inversion processes as described in the existing literature. To achieve this, we established specific criteria for the selection of POD data:

1. **Orbital Region Selection:** Satellites selected for this study were required to operate in regions characterized by high space traffic and significant thermospheric influence on spacecraft operations. This criterion ensures the method’s applicability in the most critical operational zones. As of July 2024, the majority of active satellites are located in the 350-600 km altitude range with most recorded conjunctions occurring around 500km altitude (ESA Space Debris Office, 2024), where atmospheric drag represents the predominant source of uncertainty (Mehta et al., 2017, 2022).
2. **Operational Ephemeris Dissemination:** It was essential that the ephemeris data be provided by an operational dissemination service to validate the near-real-

**Table 1.** Select List of Currently Orbiting Spacecraft and Data Sources Accessible by the Scientific Community

Spacecraft	Data Source	Number	Altitude (km)	Latency	Link
GRACE-FO-A/B, TerraSAR/TanDEM	Potsdam Geo-ForschungsZentrum	4	$\simeq 490$	30min or 2days	ftp://isdctp.gfz-potsdam.de
Swarm A-B-C	ESA Swarm Data Access Portal	3	$\simeq 460$	Daily	swarm-diss.eo.esa.int/
Planet Labs Constellation	Planet Labs Public Orbital Ephemerides Website	200+	$\simeq 475$	Unspecified	ephemerides.planet-labs.com/
Spire	NASA Commercial SmallSat Data Acquisition Program (CSDAP)	100+	$\simeq 500$	N/A	earthdata.nasa.gov/esds/csdap
Airbus Paz X-band Satellite	NASA Commercial SmallSat Data Acquisition Program (CSDAP)	1	$\simeq 514$	N/A	earthdata.nasa.gov/esds/csdap
COSMIC (Constellation Observing System for Meteorology, Ionosphere, and Climate)	UCAR Website	6	$\simeq 520-720$	Daily	data.cosmic.ucar.edu/gnss-ro
Sentinel Series	Potsdam Geo-ForschungsZentrum	7	$\simeq 700$	30min or 2days	ftp://isdctp.gfz-potsdam.de

**Table 2.** Selected Spacecraft for the Study

Spacecraft	Launch Date	De-orbit Date	Altitude	Inclination
GRACE-FO-A	22 May 2018	-	480-490km	89°
TerraSAR-X	15 Jun 2007	-	514-515km	97°
CHAMP	15 Jul 2000	19 Sep 2010	350-450km	87°

time capability of the method, thereby demonstrating its practical potential for operational use.

3. **Accessible Implementation:** To ensure the method’s feasibility for use with ephemeris streams from non-scientific entities, it is crucial that the orbit quality is derived from a POD process that is not excessively stringent. This makes the proposed method accessible and practical for a wider range of users, including those without specialized scientific expertise and/or extensive computational resources.

The ephemerides that best met these criteria were the SP3 Near-Real Time (NRT) and Rapid Science Orbits (RSO) (Schreiner et al., 2022). These orbits were used for the spacecraft listed in Table 2. The RSOs exhibit latencies of up to 2 days, while the NRT orbits have a latency of approximately 35 minutes. Satellite Laser Ranging (SLR) residuals are approximately 1-2 cm for RSO and up to 10 cm for NRT in LEO (Schreiner et al., 2022). According to Selvan et al. (2023), this level of accuracy places the RSOs within the top 20-35% of POD literature over the past two decades. This accuracy level was considered above average yet achievable, ensuring broad applicability and replicability across various satellites.

NRT orbits are subject to a maximum data transmission delay of 360 minutes. This delay represents the time interval between the satellite’s data collection and its subsequent transmission to a ground station. Upon reception at the ground station, an additional latency of approximately 35 minutes is incurred for data processing and release. Consequently, due to the timing of these transmissions, data gaps can occur, with NRT data dumps being conducted roughly 20 times per day for the TerraSAR-X/TanDEM-X satellites and 8 times per day for the GRACE-FO-A/B satellites (Schreiner et al., 2022). Thus, the minimum expected latency is around 35 minutes, assuming immediate data transmission and processing. In some instances however, the delay can extend up to 395 minutes, accounting for the combined data transmission and processing times (Schreiner et al., 2022).

While the two twin satellite pairs GRACE-FO-A/GRACE-FO-B and TerraSAR-X/TanDEM-X were initially considered in this study, results were nearly identical in every instance, providing little additional value. Consequently, the twin satellites were excluded to avoid redundancy in the dataset.

## 2.2 Selection of Storms

Geomagnetic storms are notoriously poorly characterized by empirical density models (Oliveira et al., 2021, 2017; S. Mutschler et al., 2023), yet they represent periods of significant stress on satellite operations. High-resolution data during storm events are crucial for improving existing thermospheric models in two main areas (Fang et al., 2022; Berger et al., 2023): data assimilation for live model calibration and scientific observations to enhance understanding of thermospheric behavior.

The existing literature provides limited information on the performance of POD-based inversion during geomagnetic storms. Recognizing the criticality of these periods for satellite operations, we identified storm time as a key phase to evaluate the applicability and potential of POD-density inversion.

Different categories of geomagnetic storms (G1-G5) trigger distinct physical phenomena in the thermosphere and exhibit varying signatures in density fluctuations (Knipp et al., 2021; Astafyeva et al., 2017; Laskar et al., 2023). To evaluate our method across the spectrum of storm behaviors, we identified all periods corresponding to each storm category during the operational lifetime of each satellite. For each category, we selected a minimum of 6-7 storms, if available, resulting in approximately 26 storms per satellite.

To simulate real-time conditions, ephemerides for the selected periods were programmatically retrieved from the server at runtime.

The determination of the time window for storm analysis was guided by prior findings from Oliveira et al. (2021), which noted that the thermosphere typically peaks in density approximately 12 hours following Sudden Storm Commencement (SSC) and reverts to baseline levels within about 72 hours. SSC is defined as the moment when the Bz component of the interplanetary magnetic field (IMF) sharply shifts southward.

Our method diverged from that of (Oliveira et al., 2021) in two key aspects. First, our analysis window spanned from 24 hours before to 32 hours after the storm’s maximum Kp index. Although the reduced post-storm window did not always capture the complete return to calm conditions, it sufficed for our analysis needs. This time frame provided sufficient pre-storm data to quantify relative density increases while maintaining a manageable computational load.

Secondly, our analysis centered on the time of the maximum Kp value rather than the southward turning of the Bz component. This decision was motivated by two considerations: the inherent noisiness of the Bz signal, which often requires manual annotation to identify the southward turn, and the robustness of the Kp index as a common indicator of geomagnetic activity across empirical atmospheric density models. Focusing on the Kp maximum allowed us to capture the principal phases of geomagnetic storms, providing a reliable framework for analyzing density fluctuations across different storm categories and models.

It is important to note that the indices used in the models throughout this paper are post-processed, not predicted. In practice, the discrepancy between the predicted and measured indices is significant, often contributing equally to density error when compared to modelling errors (S. Mutschler et al., 2023). Thus, the results presented here represent a lower bound of the difference between observed and computed densities.

### 2.3 Density Retrieval Methods

To provide a robust and comprehensive analysis of the proposed method, the following density retrieval methods were compared:

1. **POD-Based Density Inversion:** Our proposed method that utilizes both RSO and NRT orbits to demonstrate the operational density inversion method developed in this study on two different grades of ephemeris data.
2. **Energy Dissipation Rate (EDR)-Based Method:** This method was used to contextualize the results against another frequently used type of density inversion method (Hejduk et al., 2013; Pilinski, Crowley, et al., 2016; B. R. Bowman et al., 2005; Sutton et al., 2021).
3. **Model Densities:** Using density data from operationally available density models (JB2008, DTM2000, NRLMSISE-00), this method provided a sense of the magnitude and structure of the difference between the operational and POD-derived densities.
4. **Accelerometer-Derived Densities:** These densities served as the gold standard for comparison.[add reference and qualify with Anasuya point about winds and 2x differences]

#### 2.3.1 *POD-based density inversion*

The method utilized for density estimation from POD data is aligned with the approaches detailed in (Calabia et al., 2015; Calabia & Jin, 2017, 2021). The core premise involves numerically differentiating the POD velocities to derive accelerations, yielding

a time-series of accelerations experienced by the spacecraft. By modeling all conservative and non-conservative forces, except for drag, the residual along-track component of the acceleration can be inverted to estimate density.

Given a time series of velocity measurements from the POD process,  $V(t)$  sampled at discrete times  $t_0, t_1, t_2, \dots, t_n$ , the acceleration  $a(t)$  at time  $t_i$  can be approximated using numerical differentiation:

For  $i = 1, 2, \dots, n - 1$ :

$$a(t_i) \approx \frac{V(t_i) - V(t_{i-1})}{2\Delta t}$$

The velocities in the RSOs and NRTs are available at 30-second intervals. Numerical differentiation at this resolution yielded erroneously high acceleration values due to approximation errors. To mitigate this, velocities were interpolated using a cubic spline interpolator. Interpolating at resolutions finer than 0.01 seconds provided negligible improvements.

Even with interpolation, the resulting acceleration time series exhibited noise, contaminating the estimated densities if unaddressed. Following approaches in (Calabia et al., 2015; Oliveira et al., 2017; Bezděk, 2010), a Savitzky-Golay filter (Savitzky, 1964) with a window length of 21 and a polynomial order of 7 was applied to reduce noise. In addition, filtering of non-physical density values below  $2 \times 10^{-12} \text{ kg/m}^3$  was found to improve the resolved densities greatly.

To reduce the computational burden of subsequent steps, the acceleration time series was down-sampled from a 0.01-second resolution to a 15-second resolution.

For each numerically derived acceleration in the time series, accelerations were also computed analytically using the force model described in Table 3.

Satellite motion is guided by the total acceleration experienced by the spacecraft  $\mathbf{a}_{\text{tot}}$ , which can be decomposed into the sum of conservative  $\mathbf{a}_{\text{con}}$  and non-conservative accelerations  $\mathbf{a}_{\text{non-con}}$

$$\mathbf{a}_{\text{tot}} = \mathbf{a}_{\text{con}} + \mathbf{a}_{\text{non-con}}, \quad (1)$$

where  $\mathbf{a}_{\text{non-con}}$  can be decomposed into effects of atmospheric drag, solar radiation pressure (srp), earth optical and thermal radiation pressure (er), thermal re-radiation (trr) and antenna thrust (at):

$$\mathbf{a}_{\text{non-con}} = \mathbf{a}_{\text{drag}} + \mathbf{a}_{\text{srp}} + \mathbf{a}_{\text{erp}} + \mathbf{a}_{\text{trr}} + \mathbf{a}_{\text{at}}, \quad (2)$$

In the following method, we compute  $\mathbf{a}_{\text{con}}$ ,  $\mathbf{a}_{\text{srp}}$ , and  $\mathbf{a}_{\text{erp}}$ , and set  $\mathbf{a}_{\text{trr}}$  and  $\mathbf{a}_{\text{at}}$  to zero in order to solve for  $\mathbf{a}_{\text{drag}}$ .

The underlying principle is that under a perfect model of the non-conservative forces, the discrepancy between computed and observed accelerations is entirely attributable to changes in atmospheric density. In practice, all errors in the along-track component of the force model affect the estimated density. Some simplifying assumptions are made in the name of computational expedience and in order to broaden the applicability of the method. We allow ourselves to ignore  $\mathbf{a}_{\text{trr}}$  and  $\mathbf{a}_{\text{at}}$  and any lift component imparted by the atmosphere as their relative contributions are typically weak and the technical and computational cost of calculating these are high (March et al., 2019; Doornbos et al., 2010). In addition, the spacecraft drag coefficient and cross-sectional area are kept constant. This was done not only to expedite the computational processing of the density estimates, but also to ensure applicability of this method to the majority of orbiting spacecraft (for which these variables are generally not well characterized).



Bezdek (2010) demonstrated the value of modelling gravitational acceleration from the Earth to high degree and order to ensure that the drag signal does not become masked by gravitational signal errors. We found that modelling the gravity field beyond degree and order 80 provided imperceptible changes to the signal.

By subtracting the modeled accelerations from the measured accelerations, we obtain a time series of drag accelerations,  $\mathbf{a}_{\text{drag}}$ . These accelerations are then computed using the classical drag equation(3):

$$\mathbf{a}_{\text{drag}} = -\frac{1}{2}C_D\rho\frac{A}{m}|\mathbf{v}_{\text{rel}}|^2\hat{\mathbf{v}}_{\text{drag}} \quad (3)$$

$$\mathbf{v}_{\text{rel}} = \mathbf{v} - \boldsymbol{\omega}_{\text{earth}} \times \mathbf{r} \quad (4)$$

- $\mathbf{a}_{\text{drag}}$  : Acceleration due to drag (vector)
- $\hat{\mathbf{v}}_{\text{drag}}$  : Unit vector in the direction of the drag acceleration
- $\mathbf{v}_{\text{rel}}$  : Vector of satellite velocity relative to the air
- $\mathbf{v}$  : Velocity vector of the satellite
- $\boldsymbol{\omega}_{\text{earth}}$  : Angular rotation rate vector of the Earth
- $\mathbf{r}$  : Position vector of the satellite relative to the Earth's geocenter

Projecting  $\mathbf{a}_{\text{drag}}$  into the unit direction of  $\mathbf{v}_{\text{rel}}$  (computed assuming a co-rotating atmosphere), the density is estimated as follows:

$$\rho = \frac{-2\mathbf{a}_{\text{drag}}m}{C_D A |\mathbf{v}_{\text{rel}}|^2 \hat{\mathbf{v}}_{\text{drag}}} \quad (5)$$

The resulting accelerations exhibited some noise and occasional non-physical (i.e. negative) values. However, applying a rolling average to the estimated density mitigated these issues. For CHAMP, a rolling-average time window of 22.5 minutes was used (1/4 orbit), while for GRACE-FO and TerraSAR-X, a 45-minute window was applied (1/2 orbit). These window lengths were determined empirically, with evidence suggesting a proportional relationship between the minimal viable window length and the strength of the drag signal (Ray et al., 2023; Siemes et al., 2024).

The method runs at 1.3 density estimates per second on a 10-core CPU laptop. For a 24 hour ephemeris sampled at 30-second intervals this results in a total run time of 36 minutes. The process is parallelizable such that the run time can be reduced to a few seconds on a larger compute cluster.

### 2.3.2 Accelerometer-Derived Densities

Accelerometer-derived atmospheric densities were obtained using Level-1B accelerometer data from the Physical Oceanography Distributed Active Archive Center (PODAAC) provided by NASA JPL. Specifically, we utilized the ACT1B and SCA1B datasets, which have undergone preliminary bias and outlier corrections, including the exclusion of phantom accelerations (Harvey et al., 2022). The ACT1B dataset provides accelerations at a 1 Hz frequency in the spacecraft-body reference frame, while the SCA1B dataset supplies the necessary quaternions to transform these accelerations into the inertial J2000 frame. Additionally, we converted the timescale from GPS time to UTC to maintain consistency across all data used in this study.

**Table 3.** Force Modelling Strategy

<b>Force Model Setup</b>
<b>Conservative Forces</b>
<b>Third Body perturbations:</b> JPL DE421 Ephemerides (Folkner WM, 2008) <b>Gravity Field:</b> EIGEN-6S4 80x80 (Förste et al., 2016) <b>Solid Tides:</b> IERS 2014 (McCarthy, 1996) <b>Ocean Tides:</b> FES 2004 (Lyard et al., 2006) <b>Relativistic Correction:</b> (Montenbruck & Eberhard, 2000) eq.3.146
<b>Non-Conservative Forces</b>
<b>Earth Radiation Pressure:</b> Knocke 1x1 degree (Knocke et al., 1988) <b>Solar Radiation Pressure:</b> Cannonball ( $C_r$ ) (Montenbruck & Eberhard, 2000) + Cone shadow model (penumbra+umbra) <b>Aerodynamic Drag Force:</b> Cannonball ( $C_d$ ) + no density (inverted-for) <b>Atmospheric winds:</b> Co-rotating atmosphere (no winds)
<b>Reference System</b>
<b>Reference Frame:</b> EME2000/J2000 <b>Precession/Nutation Frame:</b> IERS 2014 Conventions (McCarthy, 1996) <b>Polar Motion and UT1:</b> IERS C04 14 (Brzeziński et al., 2009)

**Table 4.** Spacecraft Characteristics Used in Force Modelling Process

Spacecraft	Mass (kg)	Area (m <sup>2</sup> )	$C_D$	$C_r$	Reference(s)
GRACE-FO-A	600.2	1.004	3.2	1.5	(Mehta et al., 2013)
TerraSAR-X	1230.0	2.4	2.4	1.5	(Kuang et al., 2014; Dambowsky et al., 2023)
CHAMP	522.0	1.0	2.2	1.0	(Mehta et al., 2017)

The ACT1B data offer a time series of non-gravitational accelerations, from which we subtract non-conservative forces (detailed in Table 3) to isolate the atmospheric drag signal. These accelerations are then projected along the spacecraft’s instantaneous  $v_{\text{rel}}$  to extract the drag component,  $a_{\text{drag}}$ . Following the procedure outlined in Section 2.3.1, we applied the drag equation to derive the corresponding atmospheric density,  $\rho$ .

For this analysis, we did not use a high-fidelity geometric or thermal model, such as the one developed by Siemes et al. (2023). Instead, we relied on the along-track accelerations provided by the accelerometer, using a nominal drag coefficient and frontal area value from Mehta et al. (2013). This simplified approach was considered adequate given that the drag signal derived from the POD data was not expected to capture the finer details present in the accelerometer data. Thus, the computational expense of a full-fidelity simulation was not warranted.

While accelerometer-derived densities are frequently regarded as a robust benchmark (Sutton et al., 2021; Mehta et al., 2022; S. M. Mutschler et al., 2023), it is imperative to recognize that even these measurements are not devoid of uncertainties. These uncertainties persist despite the application of advanced correction techniques and high-fidelity models. For instance, Aruliah et al. (2019) demonstrated that winds inferred from CHAMP satellite accelerometer data often exceed those obtained through Fabry-Pérot interferometry by a factor of 1.5 to 2, suggesting complexities that are not fully understood. Additionally, Doornbos et al. (2010) highlighted that the choice of wind models used in the density inversion process can alter the derived densities by up to 20%. Thus, while accelerometer data serves as the best available benchmark in many studies, one should keep in mind the the potential limitations and complexities when interpreting results derived from such data.

### 2.3.3 Energy Dissipation Rate Method

The Energy Dissipation Rate (EDR) method leverages the principle that, under two-body dynamics, the sum of the kinetic and potential energy of a satellite remains conserved. Assuming atmospheric drag primarily drives changes in this conserved quantity (Picone et al., 2005), a time series of orbital energy can be used to infer atmospheric density between each point in the time series.

While EDR methods are not the central focus of this paper, they underpin some of the most effective operational density models to date (Storz, 2002; B. Bowman, 2003) and have been foundational for many years (King-Hele & Walker, 1987). Benchmarking against this method provides valuable context by comparison with well-known works in recent literature (Hejduk et al., 2013; Pilinski, Crowley, et al., 2016; B. R. Bowman et al., 2005; Sutton et al., 2021).

This study follows the EDR method outlined in (Sutton et al., 2021), specifically focusing on the density retrieval aspect rather than the data assimilative framework.

Using positions and velocities from the SP3 RSO’s, we compute the kinetic and potential energy of the satellite at each ephemeris time step:

$$\xi = \frac{v^2}{2} - \omega_{\text{Earth}}^2 \frac{x^2 + y^2}{2} - \frac{\mu}{r} - U_{\text{nonSpherical}} \quad (6)$$

where  $\frac{v^2}{2}$  represents the kinetic energy,  $\omega_{\text{Earth}}$  is the Earth’s rotational rate,  $\frac{\mu}{r}$  is the monopole term of the gravitational potential, and  $U_{\text{nonSpherical}}$  represents the potential due to Earth’s asphericity modeled by spherical harmonic expansion. The Eigen-6S4 gravity field model was employed up to degree and order 80.

The effects of the luni-solar gravitational potential were considered using the following equation (Sutton et al., 2021):

$$\xi_{3BP} = \int_{t_0}^{t_1} \bar{a}_{3B}(\vec{r}, t) \cdot \vec{v} dt \quad (7)$$

Additional energy sources, such as Solar Radiation Pressure (SRP) and Earth Radiation Pressure (ERP), were found to make negligible changes in the EDR method and were therefore excluded, consistent with previous studies (Picone et al., 2005; Sutton et al., 2021). Solving for  $\xi$  at each time step results in a time series of orbital energy, which can be converted into an EDR time series:

$$EDR_{i+1} = \xi_{i+1} - \xi_i \quad (8)$$

Given the EDR, velocity vector, positions, drag coefficient ( $C_D$ ), cross sectional area ( $A$ ), mass, and time interval ( $dt$ ), we can compute the effective density ( $\rho_{\text{eff}}$ ).

Based on the methodology in (Sutton et al., 2021), the effective density  $\rho_{\text{eff}}$  at the  $i + 1$ -th time step is determined from the EDR:

$$EDR_{i+1} = \xi_{i+1} - \xi_i = -\frac{1}{2m} \int_{t_i}^{t_{i+1}} C_D A \rho V^3 dt = -\frac{1}{2m} \rho_{\text{eff}} \int_{t_i}^{t_{i+1}} C_D A V^3 dt \quad (9)$$

Numerically, this can be solved for  $\rho_{\text{eff}}$  as follows:

$$\rho_{\text{eff}} = \frac{2m(\xi_{i+1} - \xi_i)}{-\int_{t_i}^{t_{i+1}} C_D A V^3 dt} \quad (10)$$

### 2.3.4 Operational Density Models

Despite recent advances in state-of-the-art thermospheric density models (e.g HASDM, DTM2020, NRLMSISE-2.0), their operational use is often limited by restrictive licenses. In this study, comparisons were made against three of the best models that do not suffer from such restrictions, ensuring a comparison with the current state of practice- which is of greater relevance to satellite operators. The models selected are JB2008 (B. R. Bowman, Tobiska, et al., 2008), NRLMSISE-00 (Picone et al., 2002), and DTM2000 (Bruinsma et al., 2003).

Benchmarking our POD-derived densities values against these operational models offers a clear perspective on the types of errors operators might encounter at present and the potential improvements associated with adopting POD-based density retrieval methods.

## 3 Results and Discussion

The results presented herein are structured into three principal sections, each addressing a different spatio-temporal resolution level:

1. **Fine-Grained Comparison Over a 17-Hour Period:** This section presents a benchmarking of all methods studied against accelerometer derived densities during a moderate geomagnetic storm.
2. **Inter-satellite storm comparison:** Spanning approximately 60 hours, this analysis evaluates the inter-satellite agreement on the resolution of storm-level features using data from two satellites, TerraSAR-X and GRACE-FO-A.

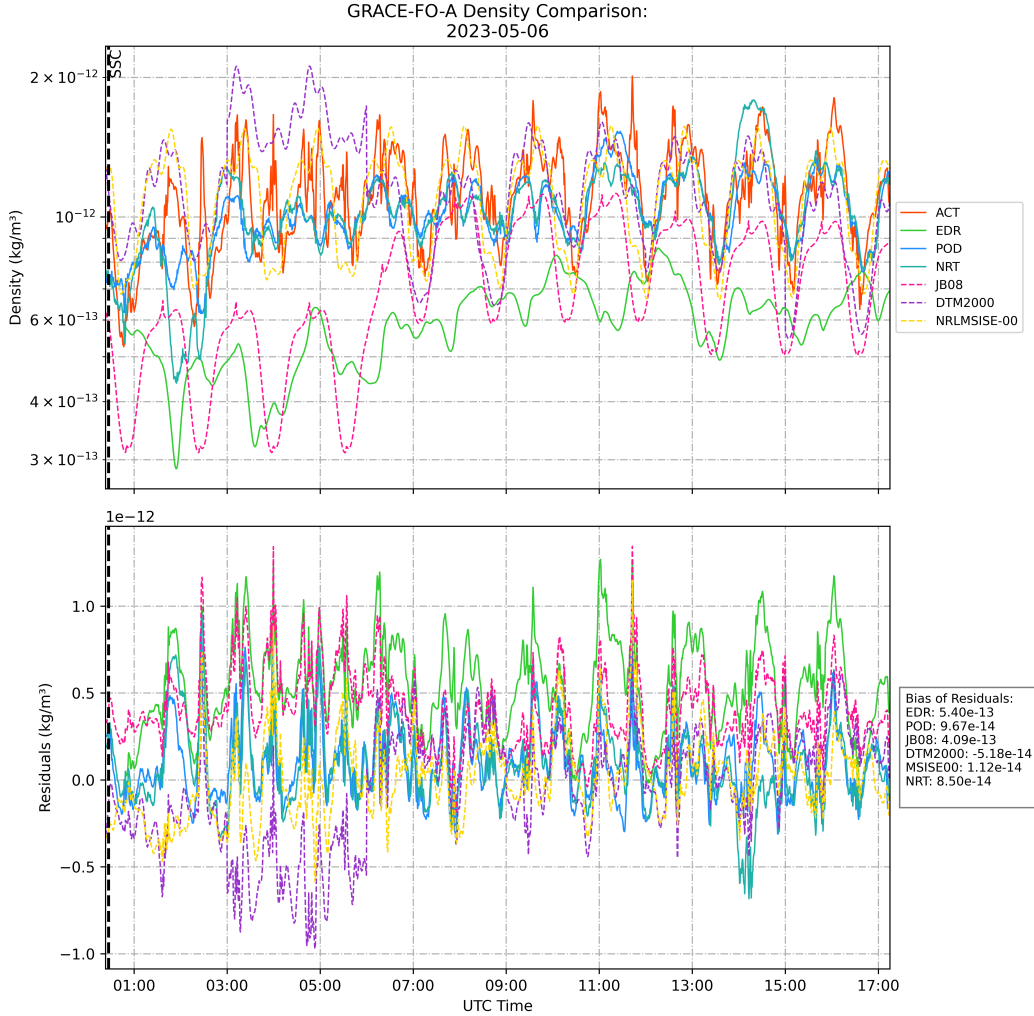


**Figure 1.** Absolute densities returned by each of the methods during the Moderate (G2) May 2023 storm period studied (top) and residuals (ACT-Modelled or Derived density) (bottom). ACT = Accelerometer, EDR = Energy Dissipation Rate, POD = POD-based method using Rapid Science Orbit, NRT = POD-based method using NRT. SSC is labelled with the black vertical dotted line(00:27 UTC).

**3. Long-Term Systematic Comparison:** This section provides a comprehensive comparison of the POD-based method’s performance relative to operational model densities over 80 storms, using data from three satellites: GRACE-FO-A, TerraSAR-X, and CHAMP.

### 3.1 Benchmarking Against GRACE-FO Accelerometer Data

Figure 1 displays the densities resolved by each method evaluated in this study over a 17-hour period during the May 2023 G2 geomagnetic storm. While this period does not capture the entire storm duration, it allows for a focused analysis of finer spatio-temporal resolution features, particularly those occurring within a single orbital revolution. These features exhibit variability beyond the typical diurnal patterns commonly addressed by most models. Notably, this period corresponds to a relatively low-drag environment, where

the acceleration due to drag hovers between  $6 \times 10^{-8} \text{ m/s}^2$  and  $1.5 \times 10^{-7} \text{ m/s}^2$ . When comparing to other studies (Ray et al., 2023), it becomes evident that this environment is at the edge of what POD density inversion techniques are capable of resolving. Consequently, the performance of the POD solution presented in the figure is likely on the lower end of the method’s potential, and one should anticipate improved performance in higher drag environments.

None of the methods fully capture the detail and fluctuations observed in the accelerometer-derived densities. Among the POD methods, NRT and RSO demonstrate broad similarity, with the exception of notable divergences at 0200, 1100, and 1400 hours. This is to be expected, as RSO benefit from more comprehensive post-processing. The differences between RSO and NRT-derived densities are relatively minor beyond these isolated instances, considering the rapid availability of NRT orbits. This points to the operational potential of the lower latency (and accuracy) orbit solutions.

Focusing on model-derived densities, NRLMSISE-00 is the least biased and most synchronized in terms of amplitude of the twice-per-rev signal, though it occasionally misses features altogether (e.g., at 0400 and 0600 hours), that DTM2000 shows some attempt at capturing. However DTM2000 over-predicts density at the storm’s onset. In contrast, JB08 consistently under-predicts density and exhibits a lag in its response to increasing density.

In the top plot of figure 1, the EDR-based density time series method displays a relatively slow, progressive rise in density. While it captures the relative increase in density, the twice-per-rev signal is sometimes out of sync with the changes observed in the accelerometer data (e.g., at 0600). It is not clear why this lag occurs, it is possible that the effects of drag may take some time to manifest at a noticeable level in the energy level of the satellites. Additionally, the EDR-derived density is positively biased throughout.

The POD-based method effectively captures the largest features of the density fluctuations. However, the magnitude of the twice-per-rev signal is attenuated relative to model-derived densities. It is interesting to note that it effectively captures some of the more irregular features of in the density signal which JB08 and NRLMSISE-00 fail to capture (e.g., at 0400 and 0600). This suggests that while the magnitude of the density peaks and troughs may be underrepresented, the finer details and irregularities are better represented by the POD method.

The residuals plot in Figure 1 indicates that the largest discrepancies towards the beginning of the storm (0200-0500), with errors ranging between  $\pm 1\text{e-}12 \text{ kg/m}^3$  for all solutions. A noticeable twice-per-rev periodicity in the error of all density retrieval sources is observed, which diminishes over time. In the later phases of the storm (0600-1700 hours), the models converge, with POD and NRLMSISE-00 and DTM2000 offering the smallest and least biased residuals, maintaining errors around  $\pm 0.5\text{e-}12 \text{ kg/m}^3$  even during the storm phase.

Analysing the time series from a spectral perspective (figure 2) illustrates that the NRLMSISE-00 model more accurately captures the dominant large-scale features of the density signal, as evidenced by its higher amplitude values at lower frequencies (left-hand side of the graph). Notably, aside from the first significant peak at approximately  $3.5 \times 10^{-4} \text{ Hz}$  and a smaller one at  $1.5 \times 10^{-4} \text{ Hz}$ - corresponding to the periodicity of half an orbit revolution and a full orbit revolution, respectively, the NRLMSISE-00 and POD data align closely. However, at higher frequencies, the POD data remains closer to the ACT values, indicating an increased level of detail in the signal. Additionally, the POD/NRT data better captures the amplitude of the signal at around  $5 \times 10^{-4} \text{ Hz}$  and  $9 \times 10^{-4} \text{ Hz}$ . Overall the POD solution provides an improvement over the EDR method for all

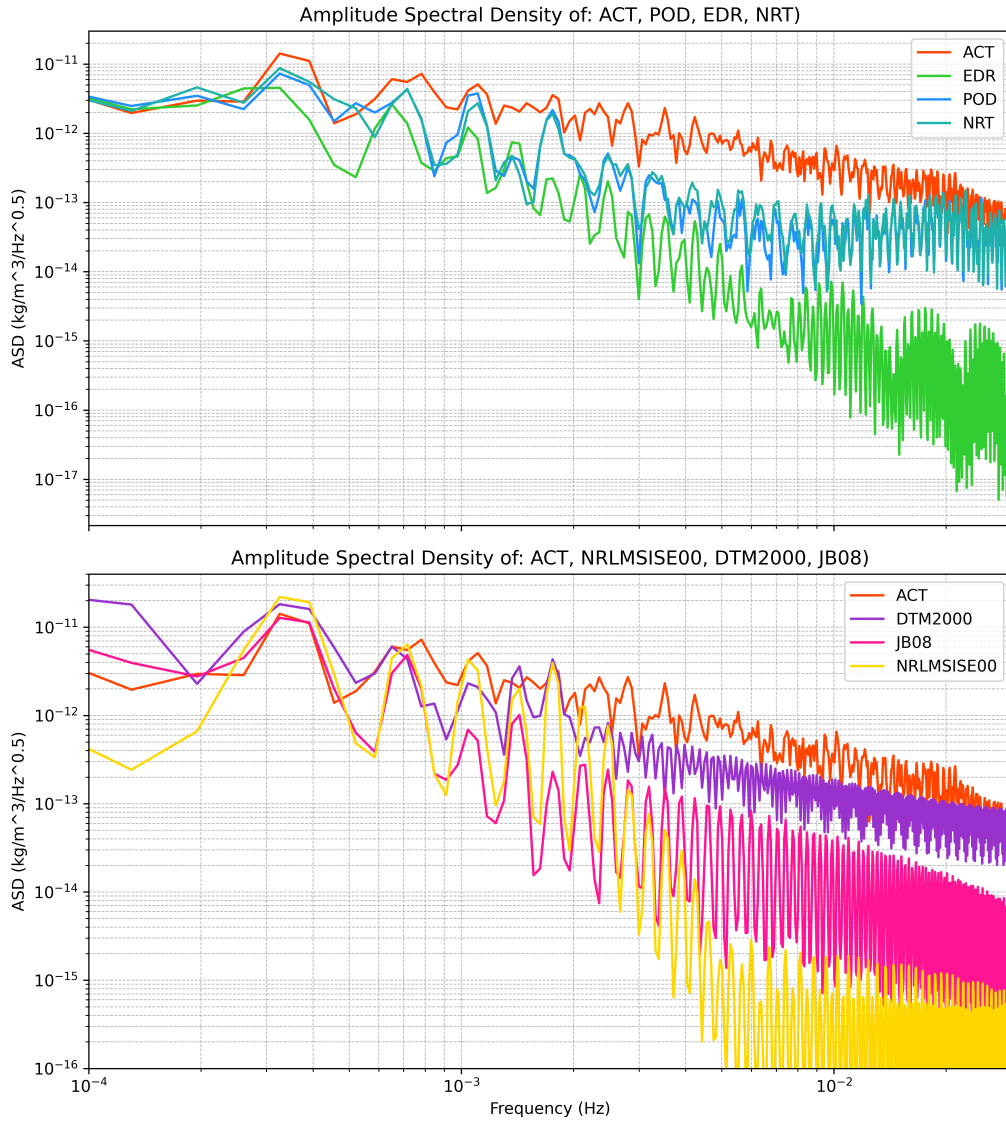


**Figure 2.** Amplitude Spectral Density of the each of the density retrieval methods during the May 2023 storm in figure 1. The top graph includes measured densities and the bottom graph includes model densities.

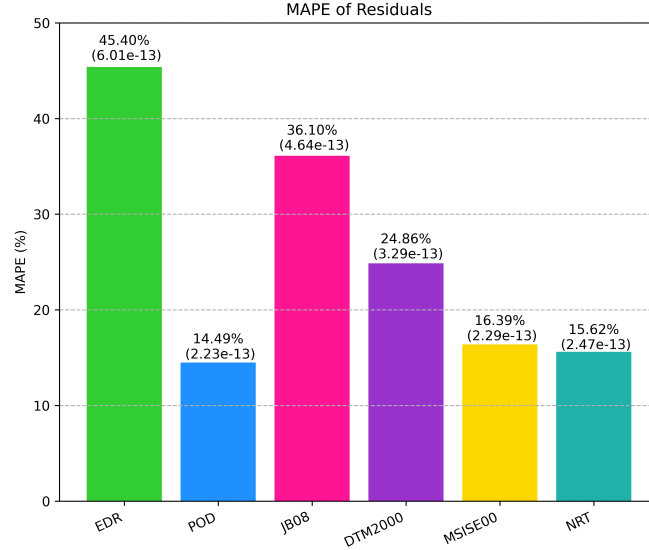


**Figure 3.** Mean Average Percentage Error (MAPE) and Root Mean Square Error (in brackets) of each method tested relative to accelerometer-derived densities

frequencies- indicating better representation of the periodic signal of the atmospheric drag experienced by the satellite.

To succinctly compare the performance of the methods, we evaluate the Mean Average Percentage Error (MAPE) and the bias of the residuals for each approach, using accelerometer-derived densities as the reference (Figure 3). MAPE provides a robust metric for assessing relative performance, particularly effective for density models where biases can be mitigated through estimation strategies. The EDR method shows a 103.37% increase in MAPE compared to the POD solution. The JB08 method exhibits a 85.43% increase, the DTM method a 52.73% increase, and the MSISE00 method a 12.31% increase. The POD, NRT, and MSISE00 models demonstrate superior agreement with the accelerometer-derived density values. The magnitude of the bias residuals serve as a proxy for how well the mean storm density was resolved. Consistent with later sections (3.2 and 3.3) we find that DTM2000 and MSISE00 perform well in this respect but the POD and NRT methods remain superior in resolving finer detail.

Energy Dissipation Rate-based methods are a stream of “live” input data that has been leveraged with great success. However, moving forward, we advocate for the use of POD-based density estimates as these are more responsive to sudden changes in the thermosphere. Enabling the use of data that is of increasingly fine spatio-temporal resolution will enable assimilation of higher-resolution EDR density observations into operational density models, as compared to commonly used EDR-based density retrieval methods on TLEs (Storz et al., 2002).

It should be noted that whilst NRLMSISE-00 performed well in figure 1, it does not respond to the geomagnetic storm thus providing a poor estimate of its relative behaviour. We believe the good performance of MSISE-00 relative to other models is somewhat coincidental in this instance, and largely driven by the fact that the model was already set at the correct density prior to the storm onset. This argument is further supported in sections 3.2 and 3.3.



Overall, on shorter timescales ( $\geq 100$  minutes), the primary downfall of the proposed method is the incomplete representation of the full amplitude of the density variation experienced by the satellite (see figure 1). This loss of detail may be due to the mismodelling of the cross-sectional area exposed to the oncoming flux (Mehta et al. (2017) indicated the area may change on the order of 46% for GRACE-FO and 11% for CHAMP) and/or the process of averaging of data points. This issue is likely to improve with shortening of the data arcs over which averaging is performed or by improved modelling of the cross sectional area of the spacecraft with the oncoming flux.

### 3.2 Density Estimates From Two Satellites During The Same Storm

Frequent attempts are made at improving agreement between thermospheric density models (Licata et al., 2020; B. R. Bowman, Kent Tobiska, et al., 2008; Mehta et al., 2022) by focusing on long-term metrics, often under the assumption that smaller-scale variations average out (Sutton, 2018; Xu et al., 2011). The resolution of smaller-scale horizontal features of the thermosphere is of increasing operational relevance, as illustrated by the connection between low resolution of models and the recent uncontrolled decay of 38 Starlink satellites (Fang et al., 2022). The operationalization of physics-based models is likely to provide significant support in tackling this issue, but will still require high spatio-temporal density observations for validation and data-assimilative purposes.

This section presents the density values retrieved by two satellites using the POD-based method and compares them to model-derived densities during over the course the April 2023 G4 Geomagnetic Storm (figure 4). The aim is to ascertain the potential of the POD-based density retrieval in resolving storm-scale features- e.g. time of storm onset, post-storm cooling rate, magnitude of increase in density and other major fluctuations within the drag signal.

Due to the occasional gaps in the NRT orbits and the findings in Section 3.1 indicating the similarity in the quality of density retrieval between RSO and NRT orbits, RSOs are utilized in the following sections to provide a continuous density estimate over the studied storm periods- however we believe the NRT are likely to produce similar results.

Prior to the storm onset ( $\simeq 1700$  on 23 April), all solutions are broadly in phase, albeit with some bias relative to one other. Similarly to Figure 1, the POD solution exhibits a reduced amplitude. The instantaneous response of DTM2000 to the increase in the Kp index at 1800 on 23 April is clear (Bruinsma et al., 2003), as is the dependence of JB08 on the Dst index when values fall below -75 nT (B. R. Bowman, Kent Tobiska, et al., 2008). One should also note the unresponsive nature of NRLMSISE-00 derived densities during this storm, with the exception of a small increase on the 23rd at midnight, attributable to its reliance on daily resolution indices (F10.7).

Both spacecraft display good temporal synchronicity in recording features across the storm lifetime: an initial 2x increase in density from 1800 to 2200, followed by a brief decrease to near pre-storm density levels for half an orbital revolution, after which the density gradually rises throughout the storm to reach a roughly 3x increase relative to pre-storm densities. Additionally, both spacecraft exhibit a strong peak at the end of the storm, which is not reflected in any of the models. Notably, the post-storm density decrease is steeper in both POD-based solutions compared to the computed densities. Finally, it is interesting to note that at the storm's peak, the sinusoidal pattern in the density signal becomes less distinct, reminiscent of the chaotic behavior observed in the accelerometer-derived densities in Figure 1.

JB08, despite its consistent low bias, captures relative changes well during storm conditions. NRLMSISE-00, although less biased, remains unresponsive to storm-time fluctuations due to its reliance on daily indices (F10.7). DTM2000 falls between these two-

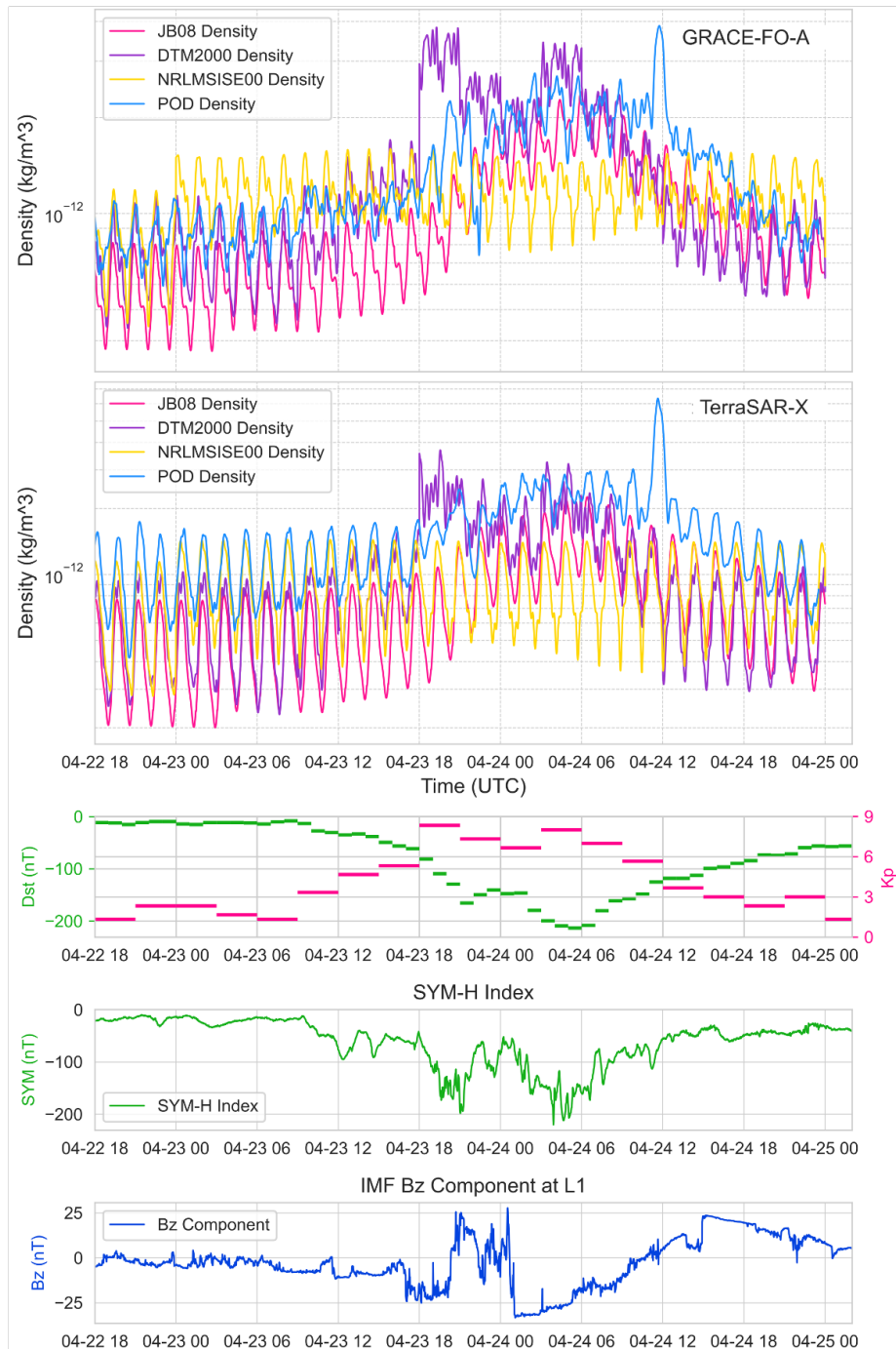


**Figure 4.** Comparison of densities retrieved using the POD-based density retrieval method and three different density models over the same G4 storm by GRACE-FO ( 477 km altitude) and TerraSAR-X ( 515 km altitude). The three bottom sub-plots include relevant space weather indices: Hourly Disturbance Storm Time (Dst), Symmetric-Horizontal Index (SYM-H), Planetary K-index (Kp), and Interplanetary Magnetic Field Z-component as measured at Lagrange Point 1 by the DISCVR satellite. F10.7 remained at 150 solar flux units throughout.

not as responsive as JB08 but less biased than NRLMSISE-00. The chronic underestimation but good variance explanation by JB08 makes it a clear candidate for data-assimilative models, as a bias correction would bring it into strong agreement with the in-situ POD-derived density.

Accepting inter-satellite agreement not only as a proxy for replicability, but also precision, we can see that no model effectively captures the storm scale changes reflected in the POD-derived densities: the initial increase in density is perhaps best captured by JB2008 although no solution captures the density dip at  $\simeq 2200$ .

Comparing the POD-derived density solution against model densities across many storms (80 in this case) enables an understanding of the biases and systematic discrepancies present in the models on a longer time scale. Whilst part of the observed-computed discrepancy can be explained by the reduced amplitude of the POD solution, this tends to be relatively consistent, and the error will also contain signal pertaining to the mis-modelling of thermospheric features that are captured by the indirect measurement, and will provide a sense of the responsiveness and spatio-temporal resolution of each model.

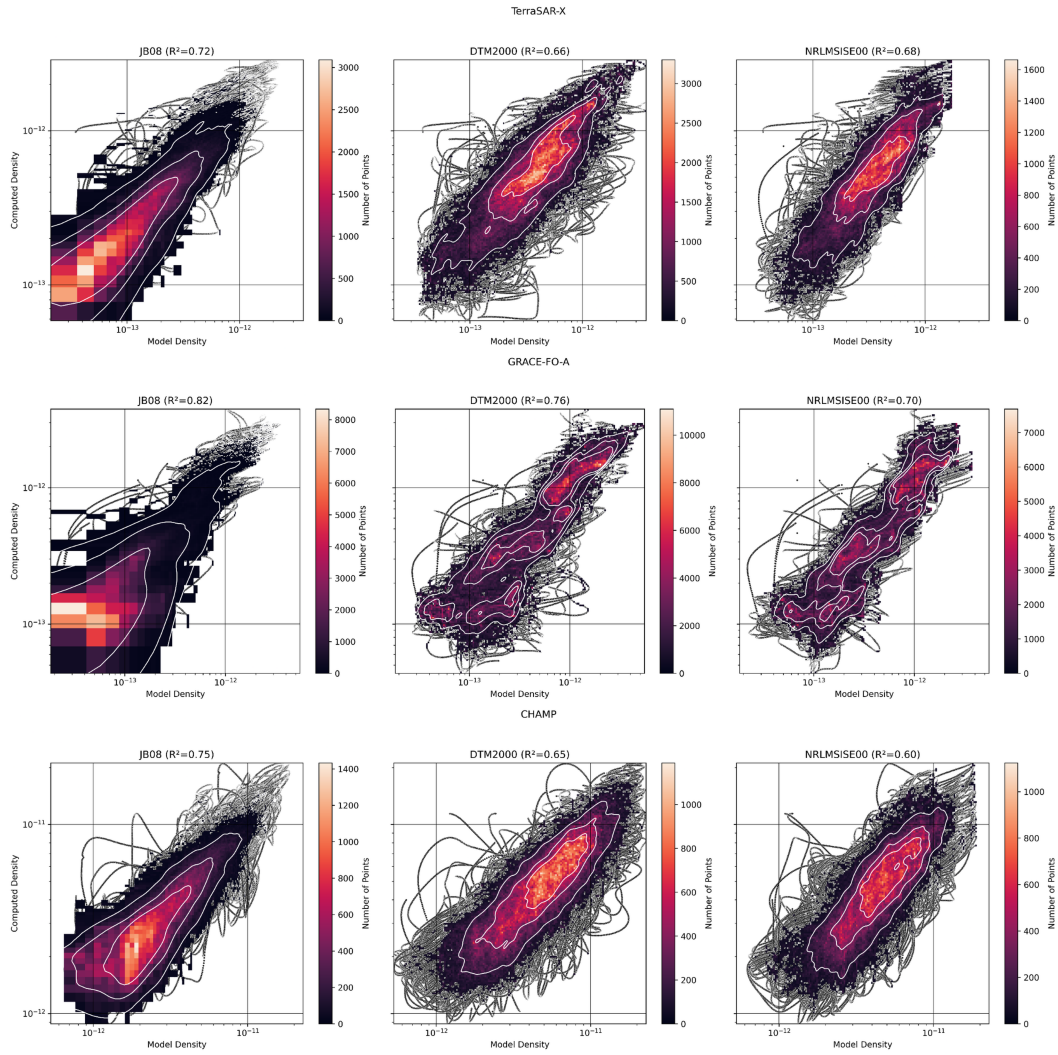
### 3.3 Comparing Density Estimates Across All Storms to Operational Density Models

Figure 5 displays, for each satellite (one per row), and each model (one per column) a comparison to the POD-derived density at every time step over all the storms. Perfect agreement between both methods would result in a straight 1:1 line. Looking at figure 5, the variance in the data is best explained by JB08 in all cases, followed by DTM2000, and then MSISE-00. The worst model disagreement was observed with NRLMSISE-00 for CHAMP ( $r^2 = 0.6$ ), whereas the best was JB08 for GRACE-FO-A ( $r^2 = 0.82$ ). Interestingly, the differences between POD derived densities and both DTM2000 and MSISE-00 appear relatively normally distributed, while the JB08 distributions are skewed towards the lower left of the plot, indicating a negative bias in the model densities relative to the observed densities. Overall this is consistent with our previous analysis in section 3.2 suggesting that JB08 captures spatio-temporal resolution well, but provides a negatively biased solution.

Density values for CHAMP are roughly one order of magnitude greater than those of GRACE-FO-A and TerraSAR-X because of its lower altitude (350-426 km compared to 477-517 km and 500-517 km respectively). Despite this, the model-to-measured density differences remained of a similar order and shape as those observed for the other two satellites. In figure 5, the GRACE-FO plots appear less Gaussian. We suspect this may be due to its very low area-to-mass ratio (0.0017), resulting in a relatively low signal-to-noise ratio in the drag signal (Ray et al., 2023) particularly in the calmer storm phases.

The model-to-measured correlations observed across all the storms (ranging from 0.60 to 0.82) are generally similar to those recorded between indirectly-measured densities for CHAMP and GRACE-FO-A and TIE-GCM densities in Sutton (2018), which reported correlations of 0.754 and 0.726, respectively. Although their analysis extended to cover non-storm periods. In Figure 5, several noteworthy observations emerge. The broadly linear correlation between all modeled and POD-derived densities indicates agreement between the models and the POD method in the representation of the first-order variations. However, JB08 always outperforms DTM2000 and NRLMSISE-00 in explaining the variance beyond this first order pattern. This is likely attributable to the spatio-temporal resolution inherent to each model can utilize: JB08 uses hourly  $D_{ST}$  during storm time (for  $D_{ST} \leq 75nT$ ), DTM2000 relies on 3-hourly Kp, and MSISE-00 uses daily indices (i.e. F10.7).

Testing the method over many storms and across three satellites further demonstrates the operational robustness of the method. The ability of this method to resolve



**Figure 5.** Scatter plots comparing model-derived and POD-derived densities across 80 storms for GRACE-FO-A, TerraSAR-X, and CHAMP. Rows represent satellites, and columns represent density models. The y-axis shows POD-derived densities, and the x-axis shows model densities at matching latitude, longitude, altitude, and time points.

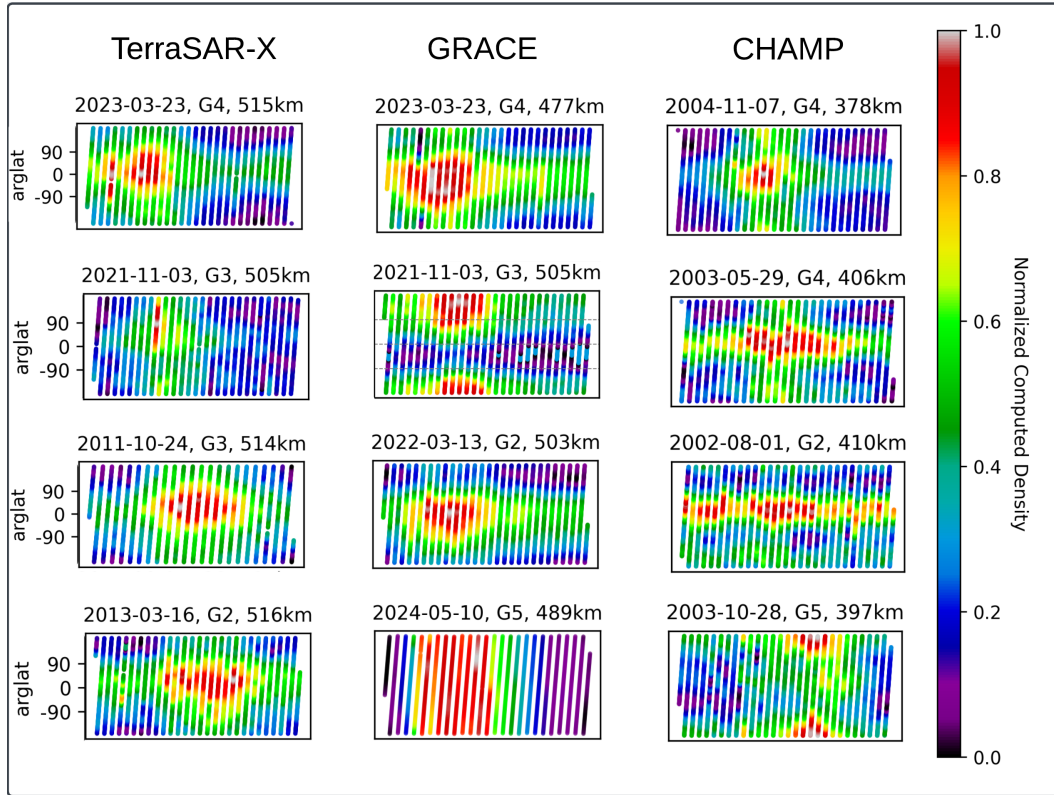


**Figure 6.** Relative Density for each a selection of storms for each satellite. Y-axis represents the satellite argument of latitude. Each line (from top to bottom) can be interpreted as one orbital revolution. Each storm is labelled with the date, NOAA storm category and satellite altitude at the start of the storm. Each plot starts at Max Kp-12hrs and ends at Max Kp +32hrs. Colour represents relative density change within each storm period.

the structure of many storms consistently is best showcased in figure 6. Inspecting the resolved density profiles of all of the storms in relative terms for one satellite provides an illustration of the resolution that is made available by the application of this method- and the variety of storm profiles that can be resolved. Each of the storm phases is clearly visible and marked by a clear day/night difference (arglat=0 being day and 180 being night), the storm commencement, peak and cooling periods are captured well in most cases, with some of weaker G1 storms showing less clearly defined structure.

Overall, the method proved robust in its ability to resolve features of the storm that models missed over a wide range of storms. By reconstructing density profiles during 80 geomagnetic storms, we demonstrated the method’s robustness in capturing distinct thermospheric features often missed by traditional models. The full set of storm profiles and the data used to produce these is provided in the accompanying code repository. This robustness is crucial for improving space weather forecasting and mitigating the risks associated with storm-induced density variations.

## 4 Conclusions

This study builds upon the POD-based density inversion methods developed by previous researchers (Calabia et al., 2015; Kuang et al., 2014; Ray et al., 2023; van den IJssel et al., 2020) by leveraging freely available LEO spacecraft ephemerides to provide high spatial resolution (sub 1/2-revolution detail), low-latency ( 35-40min) observations of thermospheric density.

We applied our method to three satellites operating at altitudes between 350 km and 515 km during 80 geomagnetic storms. The proposed technique is applicable to any satellite with ephemeris data of positional accuracy below approximately 10 cm RMS, depending on the strength of the drag signal. This broad applicability offers the potential to enhance global, near-real-time monitoring of thermospheric density at altitudes critical to most current active satellite missions, significantly contributing to our capacity to observe and respond to space weather impacts across diverse orbital regions.

A 17-hour arc against high-fidelity accelerometer-derived densities during the March 2023 G2 storm showed that our method outperformed JB2008 (78.35%), DTM2000 (49.42%), and NRLMSISE-00 (2.33%) in terms of mean average percentage accuracy.

Our method also demonstrated high computational efficiency, processing 1.5 million density estimates in under 24 hours on a university supercomputer using 100 cores. With a latency ranging from a few seconds to tens of minutes, our approach improves upon traditional density-retrieval techniques, which have delays ranging from several hours to days. For operators with access to near-real-time ephemeris data, this can enable density estimates that are almost as fast as their POD solution .

In conclusion, the proposed POD-based density inversion method is robust, having been validated across numerous storms, and accurate, outperforming traditional models when benchmarked against accelerometer-derived density. It is also open-source, with no restrictions on its use in an operational context, and functional in near-real-time, as demonstrated by its application to GFZ Potsdam SP3-C NRT and RSO orbit streams. This combination of attributes positions our method as a valuable tool for advancing thermospheric density modeling and enhancing operational capabilities.

## 5 Limitations

The proposed method has been tested exclusively using RSO and NRT orbit data provided by GFZ- a well-characterized source of precise LEO spacecraft ephemerides. Its performance with other sources of POD data remains untested, and variability in data

quality and latency from sources beyond the GFZ FTP server could limit its applicability, especially in low drag SNR environments.

This study did not attempt to optimize the SNR in the returned densities, despite evidence from previous research suggesting a clear link between these variables (Ray et al., 2023). Adaptive methods, such as changing the averaging window size as a function of the signal-to-noise ratio, could potentially resolve finer features in the density signal. Numerical methods such as Kalman smoothing have also been shown to be effective in mitigating some of this noise (van den IJssel et al., 2020).

Moreover this study has made use of low fidelity “cannonball” spacecraft models (assuming a constant cross-sectional area), which will introduce errors. While this simplification is less impactful for broadly rectangular satellites with consistent orbit-normal orientations (such as GRACE-FO-A/B), more detailed geometric models would enhance the accuracy of the resolved densities (Doornbos, 2011). The lack of uncertainty quantification, as highlighted by other studies (Siemes et al., 2024), also represents a limitation, as does the exclusion of wind effects (Siemes et al., 2023).

## Future Work

As transparency in global SSA and STM practices continues to advance, the incorporation of POD data from commercial operators such as Spire (as demonstrated in recent studies (Sutton et al., 2021; S. M. Mutschler et al., 2023)), presents a significant opportunity. The methodology outlined in this study can be integrated into these data streams. Future work will focus on applying the method to these growing data streams, and assimilating the resulting density estimates into existing density models, thereby enhancing the accuracy of density model now-casting and validation.

## Open Research Statement

The data supporting the findings of this study are openly available from the following sources:

The POD data used in this study can be accessed from the GFZ Potsdam server: <ftp://isdcdftp.gfz-potsdam.de/>. GRACE-FO-A accelerometer data is available through the Physical Oceanography Distributed Active Archive Center at NASA JPL: [https://podaac.jpl.nasa.gov/dataset/GRACE\\_L1B\\_GRAV\\_JPL\\_RL03](https://podaac.jpl.nasa.gov/dataset/GRACE_L1B_GRAV_JPL_RL03). The one-minute SYM, AE, and Dst index values can be obtained from the World Data Center for Geomagnetism in Kyoto: <https://wdc.kugi.kyoto-u.ac.jp/aedir/>. The Kp, Ap, and F10.7 indices were sourced from the GFZ Potsdam data repository: <https://kp.gfz-potsdam.de/en/data>. The IMF Bz component data was acquired from DSCOVR for 2017 onwards: <https://www.ngdc.noaa.gov/dscovr/portal/index.html#/>, and from the ACE spacecraft for the period 2000-2017: <https://izw1.caltech.edu/ACE/ASC/>. The code used for the density inversion of the GFZ POD data, along with the scripts required to reproduce the figures in this paper, can be found on GitHub: <https://github.com/CharlesPlusC/POD-Density-Inversion>.

## Acknowledgments

The authors would like to express their gratitude to Patrick Schreiner for his invaluable assistance in explaining the process by which orbits are made available on the GFZ Potsdam server. His detailed explanations of the underlying procedures and his support in helping us access the data were instrumental in advancing our research. We are deeply appreciative of his contributions.

Charles Constant and Indigo Brownhall are supported by the UK Engineering and Physical Sciences Research Council under grants EP/R513143/1 and EP/W524335/1. We gratefully acknowledge their financial support.

## References

- Arnold, D., Peter, H., Mao, X., Miller, A., & Jäggi, A. (2023). Precise orbit determination of Spire nano satellites. *Advances in Space Research*, *72*(11), 5030–5046. doi: 10.1016/j.asr.2023.10.012
- Aruliah, A., Förster, M., Hood, R., McWhirter, I., & Doornbos, E. (2019). Comparing high-latitude thermospheric winds from Fabry-Perot interferometer (FPI) and challenging mini-satellite payload (CHAMP) accelerometer measurements. *Annales Geophysicae*, *37*(6), 1095–1120. doi: 10.5194/angeo-37-1095-2019
- Astafyeva, E., Zakharenkova, I., Huba, J. D., Doornbos, E., & van den IJssel, J. (2017). Global Ionospheric and Thermospheric Effects of the June 2015 Geomagnetic Disturbances: Multi-Instrumental Observations and Modeling. *Journal of Geophysical Research: Space Physics*, *122*(11), 716–11. doi: 10.1002/2017JA024174
- Berger, T. E., Dominique, M., Lucas, G., Pilinski, M., Ray, V., Sewell, R., . . . Thiemann, E. (2023). The Thermosphere Is a Drag: The 2022 Starlink Incident and the Threat of Geomagnetic Storms to Low Earth Orbit Space Operations. *Space Weather*, *21*(3). doi: 10.1029/2022SW003330
- Bezděk, A. (2010). Calibration of accelerometers aboard GRACE satellites by comparison with POD-based nongravitational accelerations. *Journal of Geodynamics*, *50*(5), 410–423. doi: 10.1016/j.jog.2010.05.001
- Bowman, B. (2003). High Accuracy Satellite Drag Model(HASDM) review. *Advances in the Astronautical Sciences*. Retrieved from <http://www.csa.com/partners/viewrecord.php?requester=gs&collection=TRD&recid=A0427153AH>
- Bowman, B. R., Kent Tobiska, W., Marcos, F. A., & Valladares, C. (2008). The JB2006 empirical thermospheric density model. *Journal of Atmospheric and Solar-Terrestrial Physics*, *70*(5), 774–793. doi: 10.1016/j.jastp.2007.10.002
- Bowman, B. R., Moe, K., & Tahoe, L. (2005). Drag coefficient variability at 175–500 km from the orbit decay analyses of spheres. *AAS / AIAA Astrodynamics Specialists Conference, Lake Tahoe, CA, August 7-11, 2005*(AAS 05-257).
- Bowman, B. R., Tobiska, W. K., Marcos, F. A., Huang, C. Y., Lin, C. S., & Burke, W. J. (2008). A new empirical thermospheric density model JB2008 using new solar and geomagnetic indices. *AIAA/AAS Astrodynamics Specialist Conference and Exhibit*. Retrieved from <https://arc.aiaa.org/doi/10.2514/6.2008-6438> doi: 10.2514/6.2008-6438
- Briden, J., Clark, N., Siew, P. M., & Linares, R. (2022). Impact of Space Weather on Space Assets and Satellite Launches Massachusetts Institute of Technology National Oceanic and Atmospheric Administration. *Advanced Maui Optical and Space Surveillance Technologies Conference*.
- Brown, M. K., & Elvidge, S. (2024). Using WACCM-X neutral densities for orbital propagation: Challenges and solutions. *Journal of Space Safety Engineering*(xxxx). Retrieved from <https://doi.org/10.1016/j.jsse.2024.04.012> doi: 10.1016/j.jsse.2024.04.012
- Bruinsma, S., Dudok de Wit, T., Fuller-Rowell, T., Garcia-Sage, K., Mehta, P., Schiemenz, F., . . . Elvidge, S. (2023). Thermosphere and satellite drag. *Advances in Space Research*(xxxx). Retrieved from <https://doi.org/10.1016/j.asr.2023.05.011> doi: 10.1016/j.asr.2023.05.011
- Bruinsma, S., Thuillier, G., & Barlier, F. (2003). The DTM-2000 empirical thermosphere model with new data assimilation and constraints at lower boundary: Accuracy and properties. *Journal of Atmospheric and Solar-Terrestrial*



- Physics*, 65(9), 1053–1070. doi: 10.1016/S1364-6826(03)00137-8
- Brzeziński, A., Nastula, J., & Kołaczek, B. (2009). Seasonal excitation of polar motion estimated from recent geophysical models and observations. *Journal of Geodynamics*, 48(3-5), 235–240. doi: 10.1016/j.jog.2009.09.021
- Bussy-Virat, C. D., Ridley, A. J., & Getchius, J. W. (2018, 5). Effects of Uncertainties in the Atmospheric Density on the Probability of Collision Between Space Objects. *Space Weather*, 16(5), 519–537. doi: 10.1029/2017SW001705
- Calabia, A., & Jin, S. (2017). Thermospheric density estimation and responses to the March 2013 geomagnetic storm from GRACE GPS-determined precise orbits. *Journal of Atmospheric and Solar-Terrestrial Physics*, 154(March 2013), 167–179. Retrieved from <http://dx.doi.org/10.1016/j.jastp.2016.12.011> doi: 10.1016/j.jastp.2016.12.011
- Calabia, A., & Jin, S. (2021). Thermospheric Mass Density Disturbances Due to Magnetospheric Forcing From 2014–2020 CASSIOPE Precise Orbits. *Journal of Geophysical Research: Space Physics*, 126(8), 1–19. doi: 10.1029/2021JA029540
- Calabia, A., Jin, S., & Tenzer, R. (2015). A new GPS-based calibration of GRACE accelerometers using the arc-to-chord threshold uncovered sinusoidal disturbing signal. *Aerospace Science and Technology*, 45, 265–271. Retrieved from <http://dx.doi.org/10.1016/j.ast.2015.05.013> doi: 10.1016/j.ast.2015.05.013
- Codrescu, M. V., Negrea, C., Fedrizzi, M., Fuller-Rowell, T. J., Dobin, A., Jakowsky, N., ... Maruyama, N. (2012). A real-time run of the Coupled Thermosphere Ionosphere Plasmasphere Electrodynamics (CTIPE) model. *Space Weather*, 10(1), 1–10. doi: 10.1029/2011SW000736
- Dambowsky, F., Klein, K., Stefan Buckreuß, & Achim Roth. (2023). *Deutsches Zentrum für Luft und Raumfahrt: TerraSAR-X*. Retrieved from <https://www.dlr.de/de/forschung-und-transfer/projekte-und-missionen/terrasar-x/>
- Doornbos, E. (2011). *Thermospheric Density and Wind Determination from Satellite Dynamics* (Doctoral dissertation). Retrieved from [https://books.google.co.uk/books?hl=en&lr=&id=Adliku1EaJ8C&oi=fnd&pg=PR4&dq=info:sU4KcEv02JwJ:scholar.google.com&ots=ZGvWQ\\_RLlo&sig=xub-1gWGczIX-j48oJydZDeTr1s&redir\\_esc=y#v=onepage&q&f=false](https://books.google.co.uk/books?hl=en&lr=&id=Adliku1EaJ8C&oi=fnd&pg=PR4&dq=info:sU4KcEv02JwJ:scholar.google.com&ots=ZGvWQ_RLlo&sig=xub-1gWGczIX-j48oJydZDeTr1s&redir_esc=y#v=onepage&q&f=false)
- Doornbos, E., Klinkrad, H., & Visser, P. (2008). Use of two-line element data for thermosphere neutral density model calibration. *Advances in Space Research*, 41(7), 1115–1122. doi: 10.1016/J.ASR.2006.12.025
- Doornbos, E., Van Den IJssel, J., Lühr, H., Förster, M., & Koppenwallner, G. (2010). Neutral density and crosswind determination from arbitrarily oriented multiaxis accelerometers on satellites. *Journal of Spacecraft and Rockets*, 47(4), 580–589. doi: 10.2514/1.48114
- Elvidge, S., & Angling, M. J. (2019). Using the local ensemble Transform Kalman Filter for upper atmospheric modelling. *Journal of Space Weather and Space Climate*, 9. doi: 10.1051/swsc/2019018
- ESA Space Debris Office. (2024). *ESA's Annual Space Environment Report* (Tech. Rep. No. 8.0). Retrieved from [https://www.sdo.esoc.esa.int/environment\\_report/Space\\_Environment\\_Report\\_latest.pdf](https://www.sdo.esoc.esa.int/environment_report/Space_Environment_Report_latest.pdf)
- Fang, T., Kubaryk, A., Goldstein, D., Li, Z., Fuller-Rowell, T., Millward, G., ... Babcock, E. (2022, 11). Space Weather Environment During the SpaceX Starlink Satellite Loss in February 2022. *Space Weather*. Retrieved from <https://onlinelibrary.wiley.com/doi/10.1029/2022SW003193> doi: 10.1029/2022SW003193
- Folkner WM, B. D., Williams JG. (2008). *The planetary and lunar ephemeris DE 421*. Jet Propulsion Laboratory, Pasadena, California.
- Förste, C., Bruinsma, S., Abrykosov, O., Rudenko, S., Lemoine, J.-M., Marty, J.-C., ... Biancale, R. (2016). EIGEN-6S4 A time-variable satellite-only gravity

- field model to d/o 300 based on LAGEOS, GRACE and GOCE data from the collaboration of GFZ Potsdam and GRGS Toulouse. *International Centre for Global Earth Models*. Retrieved from <https://doi.org/10.5880/icgem.2016.008>
- Foster, C., Hallam, H., & Mason, J. (2016). Orbit determination and differential-drag control of Planet Labs cubesat constellations. *Advances in the Astronautical Sciences*, *156*, 645–657.
- Gondelach, D. J., & Linares, R. (2020, 2). Real-Time Thermospheric Density Estimation via Two-Line Element Data Assimilation. *Space Weather*, *18*(2), e2019SW002356. Retrieved from <https://onlinelibrary.wiley.com/doi/full/10.1029/2019SW002356><https://onlinelibrary.wiley.com/doi/abs/10.1029/2019SW002356><https://agupubs.onlinelibrary.wiley.com/doi/10.1029/2019SW002356> doi: 10.1029/2019SW002356
- Harvey, N., McCullough, C. M., & Save, H. (2022). Modeling GRACE-FO accelerometer data for the version 04 release. *Advances in Space Research*, *69*(3), 1393–1407. Retrieved from <https://doi.org/10.1016/j.asr.2021.10.056> doi: 10.1016/j.asr.2021.10.056
- He, J., Astafyeva, E., Yue, X., Pedatella, N. M., Lin, D., Fuller-Rowell, T. J., ... Kubaryk, A. (2023). Comparison of Empirical and Theoretical Models of the Thermospheric Density Enhancement During the 3–4 February 2022 Geomagnetic Storm. *Space Weather*, *21*(9), 1–24. doi: 10.1029/2023SW003521
- Hejduk, M. D., Casali, S. J., Cappellucci, D. A., Ericson, N. L., & Snow, D. E. (2013). A catalogue-wide implementation of general perturbations orbit determination extrapolated from higher order orbital theory solutions. *Advances in the Astronautical Sciences*, *148*, 619–632.
- King-Hele, D., & Walker, D. M. C. (1987). *The prediction of satellite lifetimes* (Tech. Rep.). Farnborough: Royal Aircraft Establishment.
- Knipp, D. J., Bernstein, V., Wahl, K., & Hayakawa, H. (2021). Timelines as a tool for learning about space weather storms. *Journal of Space Weather and Space Climate*, *11*. doi: 10.1051/swsc/2021011
- Knocke, P. C., Ries, J. C., & Tapley, B. D. (1988). Earth radiation pressure effects on satellites. *Astrodynamics Conference, 1988*, 577–587. doi: 10.2514/6.1988-4292
- Kuang, D., Desai, S., Sibthorpe, A., & Pi, X. (2014, 1). Measuring atmospheric density using GPS-LEO tracking data. *Advances in Space Research*, *53*(2), 243–256. doi: 10.1016/j.asr.2013.11.022
- Lal, B., Balakrishnan, A., Caldwell, B. M., Buenconsejo, R. S., & Carioscia, S. A. (2018). *Global Trends in Space Situational Awareness (SSA) and Space Traffic Management (STM)*. Retrieved from <https://apps.dtic.mil/sti/citations/AD1123106%0Ahttps://apps.dtic.mil/sti/pdfs/AD1123106.pdf>
- Larsen, P. B. (2008). Outer Space Traffic Management: Space Situational Awareness Requires Transparency. *American Insititute of Aeronautics and Astronautics*.
- Laskar, F. I., Sutton, E. K., Lin, D., Greer, K. R., Aryal, S., Cai, X., ... McClintock, W. E. (2023). Thermospheric Temperature and Density Variability During 3–4 February 2022 Minor Geomagnetic Storm. *Space Weather*, *21*(4). doi: 10.1029/2022SW003349
- Licata, R. J., Mehta, P. M., & Kent Tobiska, W. (2020). Data-Driven HASDM Density Model using Machine Learning. *AGU Fall Meeting*.
- Licata, R. J., Mehta, P. M., & Tobiska, W. K. (2021). Impact of Space Weather Driver Forecast Uncertainty on Drag and Orbit Prediction. *Advances in the Astronautical Sciences*, *175*(February), 1941–1959.
- Lyard, F., Lefevre, F., Letellier, T., & Francis, O. (2006). Modelling the global ocean tides: Modern insights from FES2004. *Ocean Dynamics*, *56*(5-6), 394–415. doi: 10.1007/s10236-006-0086-x

- March, G., Visser, T., Visser, P. N., & Doornbos, E. N. (2019). CHAMP and GOCE thermospheric wind characterization with improved gas-surface interactions modelling. *Advances in Space Research*, *64*(6), 1225–1242. Retrieved from <https://doi.org/10.1016/j.asr.2019.06.023> doi: 10.1016/j.asr.2019.06.023
- Matsuo, T., Fedrizzi, M., Fuller-Rowell, T. J., & Codrescu, M. V. (2012). Data assimilation of thermospheric mass density. *Space Weather*, *10*(5), 1–8. doi: 10.1029/2012SW000773
- McCarthy, D. (1996). IERS Conventions. *IERS Tech. Note, No. 21*, 1 - 95.
- Mehta, P. M., & Linares, R. (2018). A New Transformative Framework for Data Assimilation and Calibration of Physical Ionosphere-Thermosphere Models. *Space Weather*, *16*(8), 1086–1100. doi: 10.1029/2018SW001875
- Mehta, P. M., McLaughlin, C. A., & Sutton, E. K. (2013, 12). Drag coefficient modeling for GRACE using Direct Simulation Monte Carlo. *Advances in Space Research*, *52*(12), 2035–2051. doi: 10.1016/j.asr.2013.08.033
- Mehta, P. M., Paul, S. N., Crisp, N. H., Sheridan, P. L., Siemes, C., March, G., & Bruinsma, S. (2022). Satellite drag coefficient modeling for thermosphere science and mission operations. *Advances in Space Research*(xxxx). doi: 10.1016/j.asr.2022.05.064
- Mehta, P. M., Walker, A. C., Sutton, E. K., & Godinez, H. C. (2017). New density estimates derived using accelerometers on board the CHAMP and GRACE satellites. *Space Weather*, *15*(4), 558–576. doi: 10.1002/2016SW001562
- Montenbruck, O., & Eberhard, G. (2000). *Satellite Orbits Models, Methods and Applications* (3rd ed.). Springer-Verlag Berlin.
- Mutschler, S., Kent Tobiska, W., Pilinski, M., Bruinsma, S., Sutton, E., Knipp, D., ... Wahl, K. (2023). A Survey of Current Operations-Ready Thermospheric Density Models for Drag Modeling in LEO Operations. *Advanced Maui Optical and Space Surveillance Technologies (AMOS) Conference*(October). Retrieved from [www.amostech.com](http://www.amostech.com)
- Mutschler, S. M., Axelrad, P., Sutton, E. K., & Masters, D. (2023). Physics-Based Approach to Thermospheric Density Estimation Using CubeSat GPS Data. *Space Weather*, *21*(1). doi: 10.1029/2021SW002997
- Oliveira, D. M., Zesta, E., Mehta, P. M., Licata, R. J., Pilinski, M. D., Tobiska, W. K., & Hayakawa, H. (2021). The Current State and Future Directions of Modeling Thermosphere Density Enhancements During Extreme Magnetic Storms. *Frontiers in Astronomy and Space Sciences*, *8*(October), 1–9. doi: 10.3389/fspas.2021.764144
- Oliveira, D. M., Zesta, E., Schuck, P. W., & Sutton, E. K. (2017). Thermosphere Global Time Response to Geomagnetic Storms Caused by Coronal Mass Ejections. *Journal of Geophysical Research: Space Physics*, *122*(10), 762–10. doi: 10.1002/2017JA024006
- Picone, J. M., Emmert, J. T., & Lean, J. L. (2005). Thermospheric densities derived from spacecraft orbits: Accurate processing of two-line element sets. *Journal of Geophysical Research: Space Physics*, *110*(A3), 1–19. doi: 10.1029/2004JA010585
- Picone, J. M., Hedin, A. E., Drob, D. P., & Aikin, A. C. (2002). NRLMSISE-00 empirical model of the atmosphere: Statistical comparisons and scientific issues. *Journal of Geophysical Research: Space Physics*, *107*(A12), 1–16. doi: 10.1029/2002JA009430
- Pilinski, M. D., Crowley, G., Sutton, E. K., & Codrescu, M. (2016). Improved Orbit Determination and Forecasts with an Assimilative Tool for Satellite Drag Specification. *Advanced Maui Optical and Space Surveillance Technologies (AMOS) Conference*. Retrieved from <http://www.amostech.com/TechnicalPapers/2016/Poster/Pilinski.pdf>
- Pilinski, M. D., McNally, R. L., Bowman, B. A., Palo, S. E., Forbes, J. M., Davis,

- B. L., ... Sanders, B. (2016). Comparative analysis of satellite aerodynamics and its application to space-object identification. *Journal of Spacecraft and Rockets*, 53(5), 876–886. doi: 10.2514/1.A33482
- Ray, V., Sutton, E. K., Thayer, J. P., & Hesar, S. G. (2023). A long-term neutral density database using commercial satellite data for atmospheric model calibration Vishal Ray Kayhan Space Corp. *Advanced Maui Optical and Space Surveillance Technologies (AMOS) Conference*. Retrieved from [www.amostech.com](http://www.amostech.com)
- Robinson, J. (2016). Transparency and confidence-building measures for space security. *Space Policy*, 37, 134–144. Retrieved from <http://dx.doi.org/10.1016/j.spacepol.2016.11.003> doi: 10.1016/j.spacepol.2016.11.003
- Saunders, A., Lewis, H., & Swinerd, G. (2011). Further evidence of long-term thermospheric density change using a new method of satellite ballistic coefficient estimation. *Journal of Geophysical Research: Space Physics*, 116(10), 1–15. doi: 10.1029/2010JA016358
- Savitzky, M. J. E., A.; Golay. (1964). Smoothing and Differentiation of Data. *Anal. Chem*, 36(8), 1627–1639. Retrieved from <https://doi.org/10.1021/ac60214a047>
- Schreiner, P. A., Neumayer, K., & König, R. (2022). *GFZ Rapid Science and Near Real Time Orbit Products* (Tech. Rep.). doi: <https://doi.org/10.48440/GFZ.B103-22067>
- Selvan, K., Siemuri, A., Prol, F. S., Välisuo, P., Bhuiyan, M. Z. H., & Kuusniemi, H. (2023). Precise orbit determination of LEO satellites: a systematic review. *GPS Solutions*, 27(4), 1–17. Retrieved from <https://doi.org/10.1007/s10291-023-01520-7> doi: 10.1007/s10291-023-01520-7
- Siemes, C., Borries, C., Bruinsma, S., Fernandez-Gomez, I., Hładczuk, N., den IJssel, J., ... Visser, P. (2023). New thermosphere neutral mass density and crosswind datasets from CHAMP, GRACE, and GRACE-FO. *Journal of Space Weather and Space Climate*, 13(November 2013), 16. doi: 10.1051/swsc/2023014
- Siemes, C., Maddox, S., Carraz, O., Cross, T., George, S., van den IJssel, J., ... Visser, P. (2022). CASPA-ADM: a mission concept for observing thermospheric mass density. *CEAS Space Journal*, 14(4), 637–653. Retrieved from <https://doi.org/10.1007/s12567-021-00412-1> doi: 10.1007/s12567-021-00412-1
- Siemes, C., van den IJssel, J., & Visser, P. (2024). Uncertainty of thermosphere mass density observations derived from accelerometer and GNSS tracking data. *Advances in Space Research*(xxxx). Retrieved from <https://doi.org/10.1016/j.asr.2024.02.057> doi: 10.1016/j.asr.2024.02.057
- Storz, M. F. (2002). HASDM validation tool using energy dissipation rates. *AIAA/AAS Astrodynamics Specialist Conference and Exhibit*(January 2001). doi: 10.2514/6.2002-4889
- Storz, M. F., Bowman, B. R., & Branson, M. J. I. (2002). High accuracy satellite drag model (HASDM). *AIAA/AAS Astrodynamics Specialist Conference and Exhibit*(August). doi: 10.2514/6.2002-4886
- Sutton, E. K. (2018). A New Method of Physics-Based Data Assimilation for the Quiet and Disturbed Thermosphere. *Space Weather*, 16(6), 736–753. doi: 10.1002/2017SW001785
- Sutton, E. K., Thayer, J. P., Pilinski, M. D., Mutschler, S. M., Berger, T. E., Nguyen, V., & Masters, D. (2021). Toward Accurate Physics-Based Specifications of Neutral Density Using GNSS-Enabled Small Satellites. *Space Weather*, 19(6), 1–15. doi: 10.1029/2021SW002736
- van den IJssel, J., Doornbos, E., Iorfida, E., March, G., Siemes, C., & Montenbruck, O. (2020). Thermosphere densities derived from Swarm GPS observations. *Advances in Space Research*, 65(7), 1758–1771. doi: 10.1016/j.asr.2020.01.004

Xu, J., Wang, W., Lei, J., Sutton, E. K., & Chen, G. (2011). The effect of periodic variations of thermospheric density on CHAMP and GRACE orbits. *Journal of Geophysical Research: Space Physics*, 116(2), 1–10. doi: 10.1029/2010JA015995